"Warm Rain" in the Tropics: Seasonal and Regional Distributions Based on 9 yr of TRMM Data

CHUNTAO LIU AND EDWARD J. ZIPSER

Department of Meteorology, University of Utah, Salt Lake City, Utah

(Manuscript received 20 May 2008, in final form 29 July 2008)

ABSTRACT

How much precipitation is contributed by warm rain systems over the tropics? What is the typical size, intensity, and echo top of warm rain events observed by the Tropical Rainfall Measuring Mission (TRMM) Precipitation Radar over different regions of the tropics? What proportion of warm raining areas is actually attached to the edges of cold systems? Are there mesoscale warm raining systems, and if so, where and when do they occur? To answer these questions, a 9-yr TRMM precipitation feature database is used in this study. First, warm rain features in 20°S–20°N are selected by specifying precipitation features 1) with minimum infrared brightness temperature $> 0°C$, 2) with TRMM Precipitation Radar (PR) echo top below freezing level, or 3) without any ice-scattering signature in the microwave observations, respectively. Then, the geographical, seasonal, and diurnal variations of the rain volume inside warm rain features defined in these three ways are presented. The characteristics of warm rain features are summarized.

Raining pixels with cloud-top temperature above 0°C contribute 20% of the rainfall over tropical oceans and 7.5% over tropical land. However, about half of the warm pixels over oceans and two-thirds of the warm pixels over land are attached to cold precipitation systems. A large amount of warm rainfall occurs over oceans near windward coasts during winter. Most of the warm rain systems have small size < 100 km^2 and weak radar echo with a modal maximum near-surface reflectivity around 23 dB*Z*. However, mesoscale warm rain systems with strong radar echoes do occur in large regions of the tropical oceans, more during the nighttime than during daytime. Though the mean height of the warm precipitation features over oceans is lower than that over land, there is no significant regional difference in its size and intensity.

1. Introduction

Warm rain over tropical oceans can be from stratocumuli (Austin et al. 1996), or well-developed trade wind cumuli (Malkus 1954, 1955; Baker 1993), and usually comes in the form of shallow, isolated convective showers (Schumacher and Houze 2003). To study rain initiation, cloud processing, and the large-scale conditions of these warm rain systems, there have been several field campaigns targeting warm rain systems over oceans, such as the field campaign near Barbados, West Indies, in 1963 (Simpson et al. 1967), the Atlantic Trade Wind Experiment (ATEX; Augstein et al. 1973), the Barbados Oceanographic and Meteorological Experiment (BOMEX; Nitta and Esbensen 1974), the East Pacific Investigation of Climate (EPIC; Bretherton et al., 2004), and recently the Rain In Shallow Cumulus over the Ocean Experiment (RICO; Rauber et al. 2007).

Also there have been many efforts to evaluate the amount of nondrizzle warm rainfall and its role in the tropical water cycle by using satellite observations. These include a finding of a 14% raining area over the western Pacific Ocean as retrieved from satellite microwave radiances over areas with warm infrared brightness temperatures (Liu et al. 1995), a 20%–40% rain volume reported from gauges over land and ships collocated with warm infrared cloud tops (Petty 1999), and a 20% rainfall volume retrieved from space-borne precipitation radar over tropical oceans under columns with radar echo tops below the 0°C level (Short and Nakamura 2000). All of these satellite-based studies have one thing in common: identifying warm rainfall at the satellite pixel level. However, many of these warm raining pixels are adjacent to cold precipitation pixels (Fig. 1b), with many of them oftentimes coming from within the same precipitation feature (Fig. 1c). From the

---

Corresponding author address: Dr. Chuntao Liu, Dept. of Meteorology, University of Utah, Rm. 819, 135S 1460E, Salt Lake City, UT 84112-0110.
E-mail: liu.c.t@utah.edu

DOI: 10.1175/2008JCLI2641.1

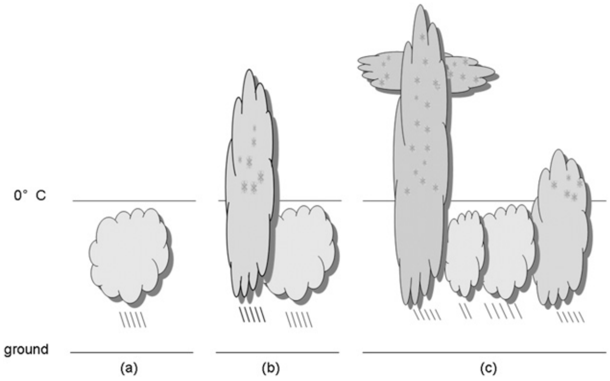

FIG. 1. Schematic diagram of warm rain events: (a) stand-alone, isolated warm rain event, (b) warm raining clouds adjacent to a cold raining system, and (c) warm raining clouds embedded in a cloud cluster.

definition in the *Glossary of Meteorology*, "warm rain is the rain formed from a cloud having temperatures at all levels above 0°C (32°F), and resulting from the droplet coalescence process." It is difficult to claim that rain at those warm pixels adjacent to the precipitation at temperatures colder than 0°C is only from the coalescence process and occurs without the involvement of ice processes. Thus, one may ask, can we still call this warm rain? For this reason, a "purer" warm rain as shown in Fig. 1a can be defined, first by grouping raining pixels into precipitation features (PFs), then making sure no cold pixels are included inside the feature (Nesbitt et al. 2006). In this study, we use a similar PF method to evaluate the importance of warm rainfall over the tropics and compare this with the amount of warm rainfall accumulated from all warm raining pixels.

Generally, nondrizzle warm rain systems are shallow, isolated, and of small size as shown in Fig. 1a and demonstrated later (see Fig. 7). However, large warm precipitation systems do exist over the tropics (Rauber et al. 2007). For example, in Fig. 2, two precipitation systems were observed from the Tropical Rainfall Measuring Mission (TRMM; Kummerow et al. 1998) satellite, with mesoscale size and a near-surface reflectivity greater than 40 dB*Z*, but a low radar echo top below the typical freezing level (4.5 km) over the tropics. The minimum infrared brightness temperatures

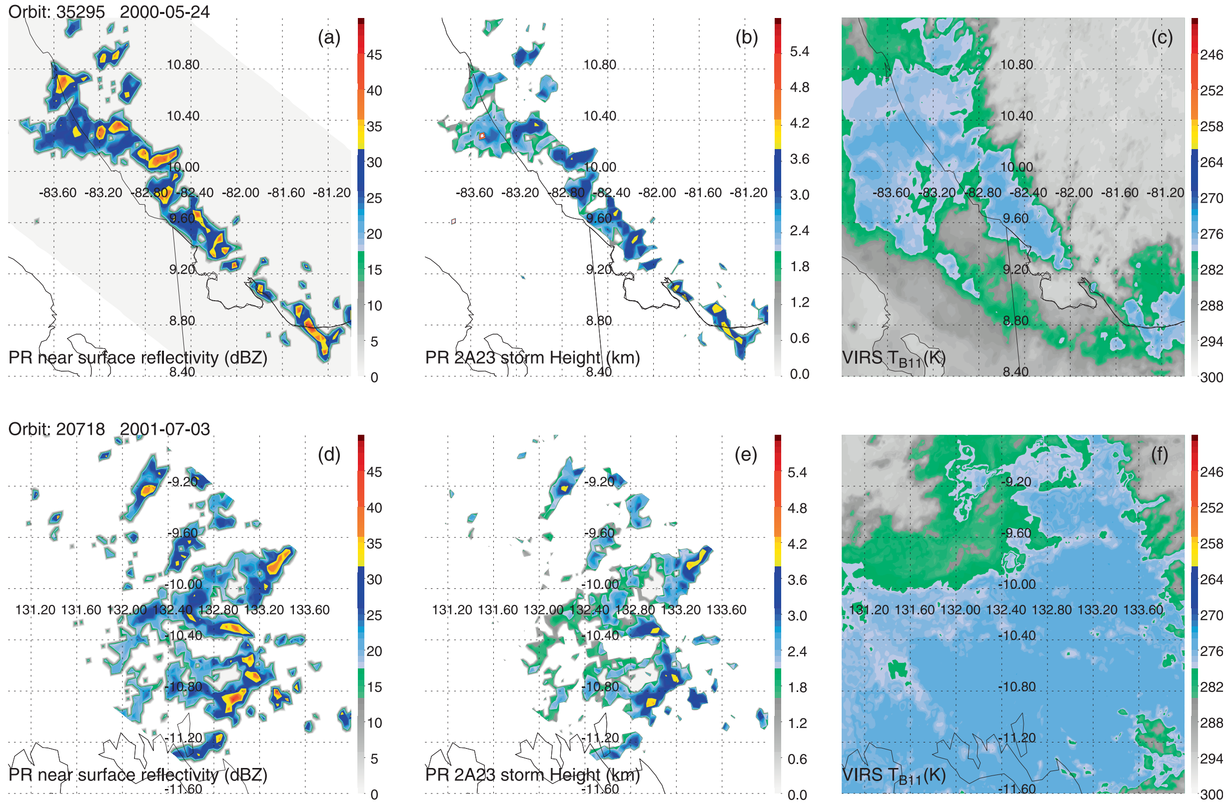

FIG. 2. Two examples of TRMM-observed warm PFs with extremely large areas. (a)–(c) The first example is a PF over the east coast of Costa Rica on 24 May 2000. This PF had an area of 6770 km^2, a maximum near-surface reflectivity of 43.6 dB*Z*, a minimum infrared brightness temperature T_{B11} value of 273.9 K, and a maximum height of 20 dB*Z* at 4 km. (d)–(f) The second example is a PF off the north coast of Australia near Darwin on 3 July 2001. This PF had an area of 10 470 km^2, a maximum near-surface reflectivity value of 47.2 dB*Z*, a minimum T_{B11} of 273.1 K, and a maximum height of 20 dB*Z* at 4.25 km.

TABLE 1. Population, raining area and rainfall contribution from the warm PFs differently defined by the PFs with a minimum VIRS $T_{B11} > 273$ K, a maximum 2A23 storm height < 4.5 km, and a minimum TMI 85-GHz PCT > 250 K. There are 38 378 154 PFs from 9 yr (1998–2006) of TRMM observations over 20°S–20°N.

	Population	Population (%)	Rain area (%)	Rainfall (%)
PFs with min $T_{B11} > 273$ K	18 590 492	48.4	13.3	8.0
PFs with max storm height < 4.5 km	24 188 648	63.0	16.6	9.5
Min 85-GHz PCT > 250 K	36 851 287	96.0	40.4	25.0

inside these systems are above 273 K. The study of these warm rain systems with mesoscale size is of interest.

This study addresses the following questions:

- How much rainfall is contributed by warm rain systems over tropical ocean and land? What is the difference between the rain contributions in the tropics from the warm pixels and those from inside the PFs that are entirely warm? In other words, how much of the "warm" rainfall is coming from pixels attached to or within raining systems with cold tops?
- What are the characteristics of the "pure" warm PFs, such as size, cloud top, and intensity observed by precipitation radar? Are there any regional differences? When and where do mesoscale warm rain systems happen?

First, 9 yr of rainfall retrievals from measurements of the TRMM Precipitation Radar (PR) are used to define the PFs. Second, we select the warm PFs if their radar echo top below freezing level, if their infrared brightness temperatures are warmer than 273 K, or if they are without a separate microwave ice-scattering signature. Based on these definitions, the contributions of rainfall from warm PFs are quantified seasonally and diurnally. Characteristics of warm PFs are summarized and the regional variations are discussed. Finally, the geographical distributions of warm rain systems with large rain volume are shown seasonally.

2. Data and methods

The PFs used in this study are from the 9-yr University of Utah TRMM PF database (Liu et al. 2008). This

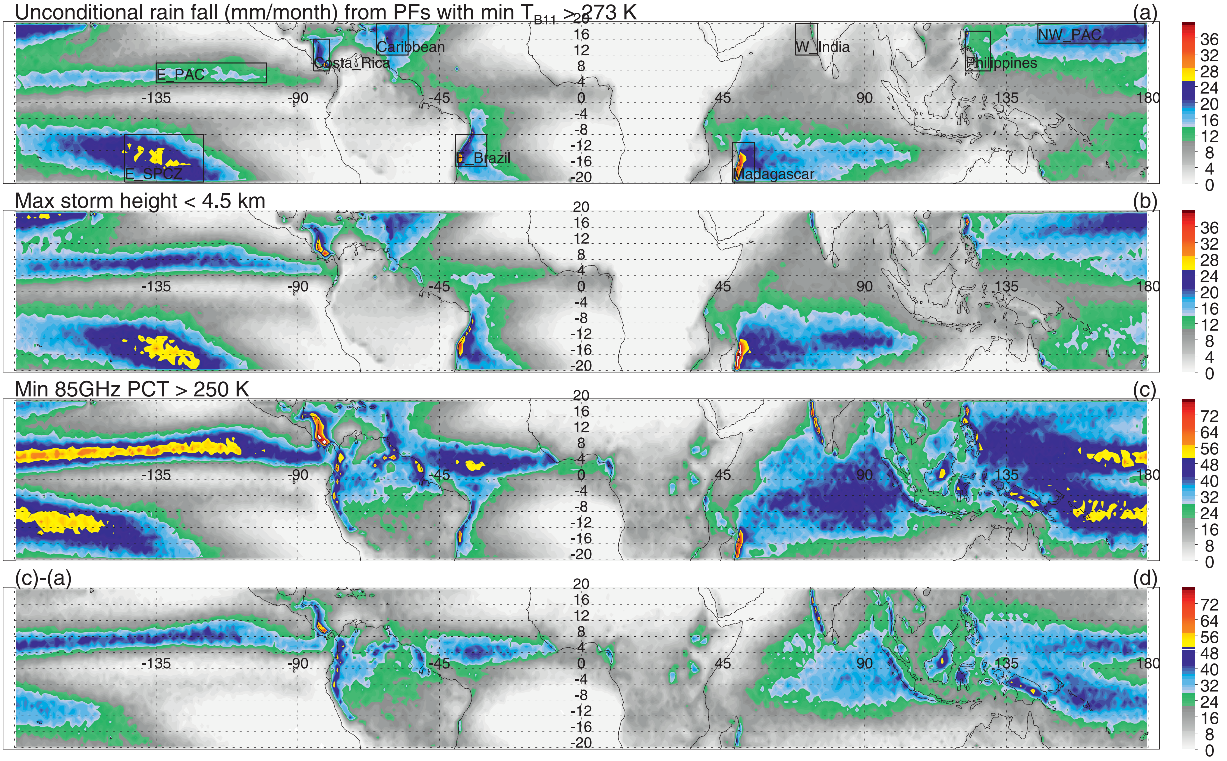

FIG. 3. Unconditional rainfall (mm month^{-1}) from PFs with (a) a minimum VIRS $T_{B11} > 273$ K, (b) a maximum PR 2A23 storm height < 4.5 km, and (c) a minimum TMI 85-GHz PCT > 250 K. (d) The differences between (c) and (a). The selected regions with high monthly rainfall from warm PFs are highlighted in (a) for regional comparisons. Note that the scales are different from (a) and (b) to (c) and (d).

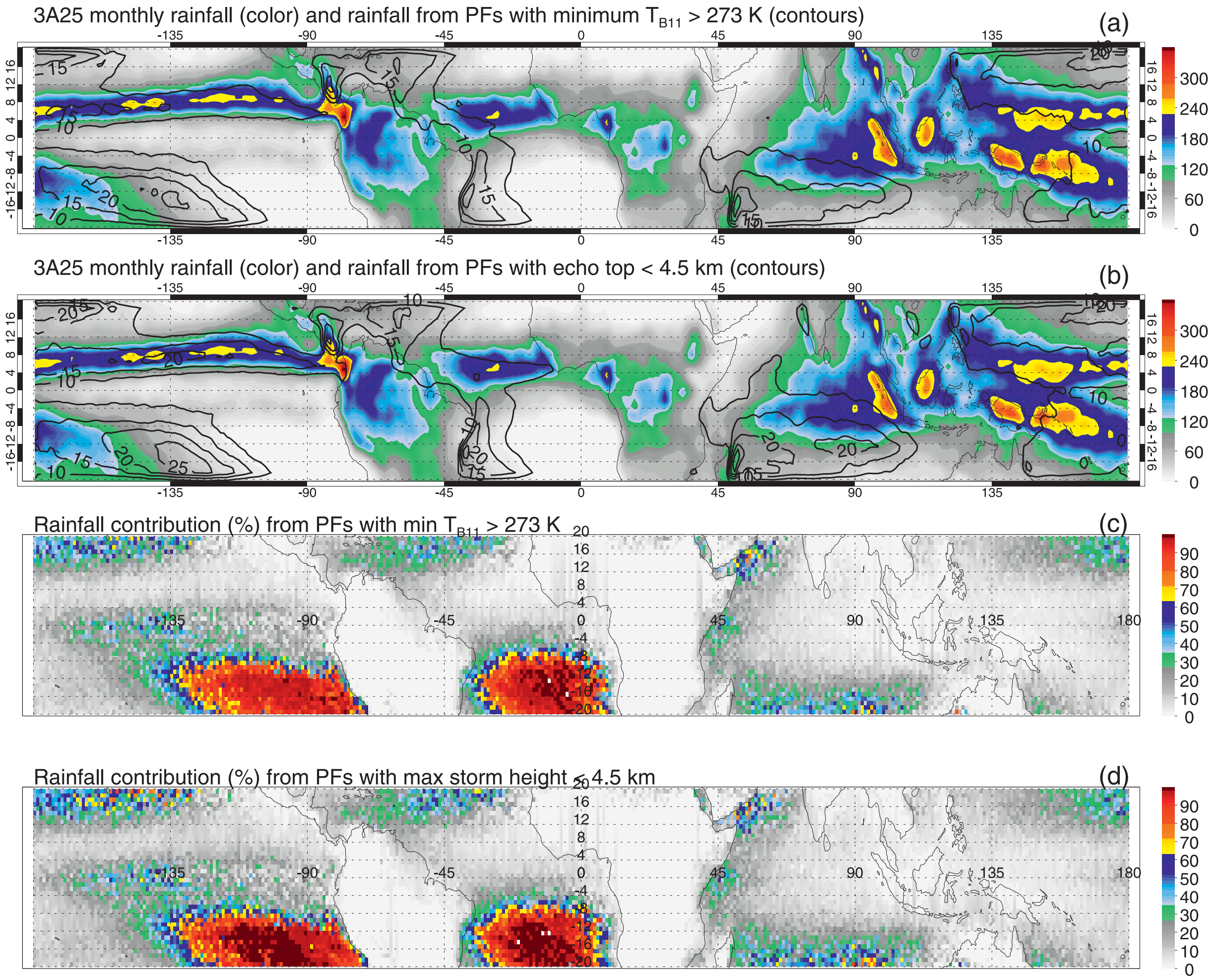
3A25 monthly rainfall (color) and rainfall from PFs with minimum T_{B11} > 273 K (contours)

3A25 monthly rainfall (color) and rainfall from PFs with echo top < 4.5 km (contours)

Rainfall contribution (%) from PFs with min T_{B11} > 273 K

Rainfall contribution (%) from PFs with max storm height < 4.5 km

FIG. 4. (a) Geographical distribution of unconditional rainfall (mm month^{-1}) from PFs (contours) with a minimum VIRS $T_{B11} >$ 273 K and the total precipitation (mm month^{-1}) from PR 3A25 (color fill). (b) Same as in (a) but for rainfall from PFs with a maximum PR 2A23 storm height < 4.5 km. (c) Fraction of rainfall from PFs with a minimum $T_{B11} >$ 273 K. (d) Fraction of rainfall from PFs with a maximum storm height < 4.5 km.

database was developed within the framework of PFs as defined by Nesbitt et al. (2000). A PF is defined by grouping the contiguous pixels with nonzero near-surface rain from TRMM PR 2A25 products (Iguchi et al. 2000). Then, the characteristics of each PF are summarized from collocated measurements and retrievals from the PR, TRMM Microwave Imager (TMI), Visible and Infrared Sensor (VIRS), and Lightning

TABLE 2. Mean unconditional rainfall, contribution of raining area, and rainfall from the differently defined warm PFs in Table 1, and for the pixels with VIRS T_{B11} > 273 K, and the pixels with TMI 85-GHz PCT > 250 K over 20°S–20°N land and ocean.

	Land			Ocean		
	Rainfall (mm month^{-1})	Rain area (%)	Rainfall (%)	Rainfall (mm month^{-1})	Rain area (%)	Rainfall (%)
PFs with min T_{B11} >273 K	2.2	4.0	2.3	9.5	16.4	10.0
PFs with max storm height < 4.5 km	3.0	6.3	3.0	11.0	20.0	11.6
PFs with min 85-GHz PCT > 250 K	18.3	32.0	18.6	25.9	43.2	27.2
Pixels with VIRS T_{B11} >273 K	7.4	12.2	7.5	19.2	30.2	20.2
Pixels with TMI 85-GHz PCT > 250 K	58.8	77.5	59.7	61.1	83.4	64.3

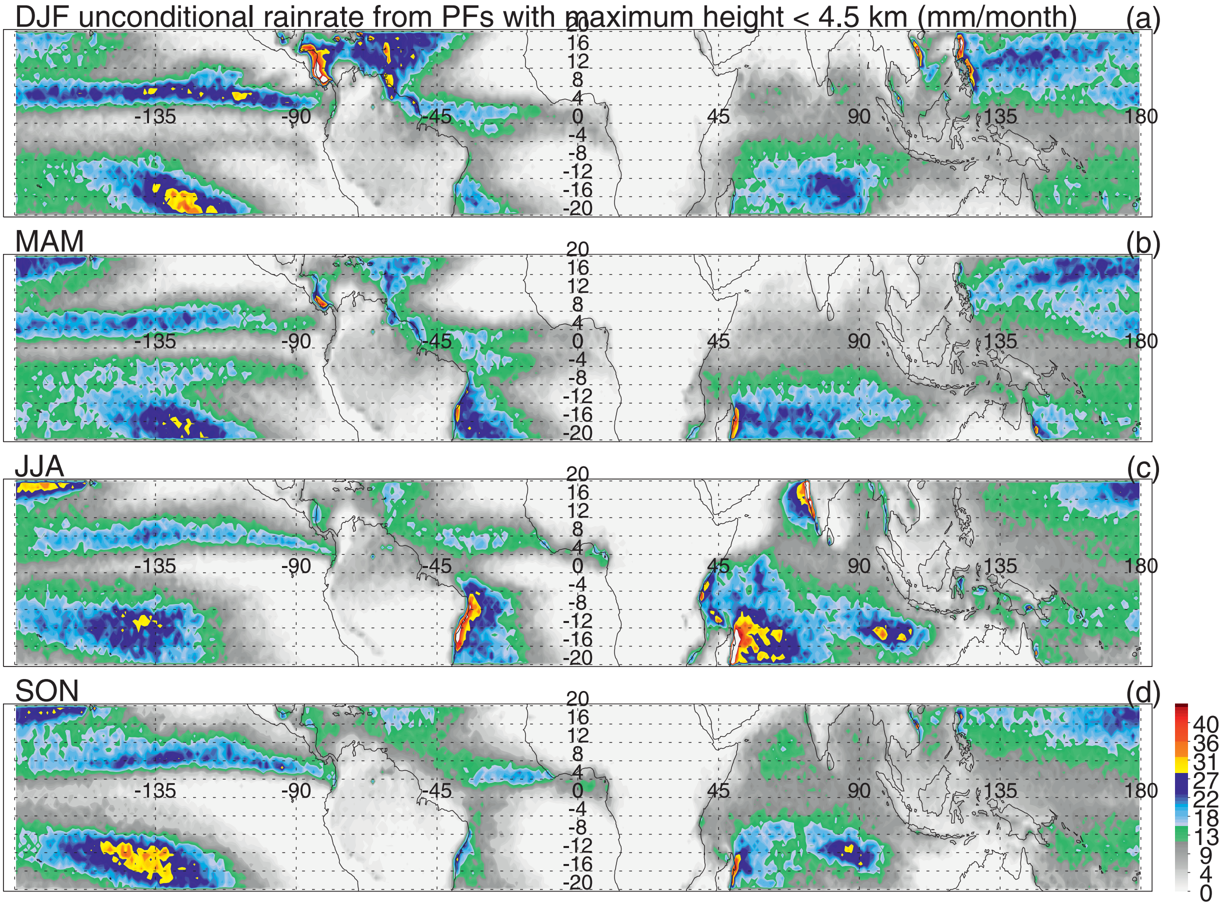

FIG. 5. Seasonal variation of the unconditional rainfall from PFs with maximum PR 2A23 storm height < 4.5 km. Units are mm month^{-1}.

Imaging System (LIS) (see details in Liu et al. 2008). The properties of the PFs used in this study include

- size, as calculated from the number of PR pixels with nonzero 2A25 near-surface rain;
- volumetric rain, calculated from 2A25 near-surface rain;
- maximum detectable echo top, defined as the maximum storm height from TRMM 2A23 products (Awaka et al. 1998); and
- minimum TMI 85-GHz polarization-corrected temperature (PCT; Spencer et al. 1989) and minimum VIRS infrared brightness temperature at 10.8-μm wavelength (T_{B11}).

More than 38 million PFs are defined over 20°S–20°N from 9 yr of TRMM data. From these PFs, we use three groups of criteria to select the warm PFs: 1) minimum $T_{B11} > 0°C$ (273 K), which eliminates all PFs with cloud-top temperatures inferred from infrared brightness temperatures higher than the freezing point; 2) maximum PR echo top below 4.5 km, the typical freezing level over the tropics, which should assure that all large precipitation particles in the PF detected by the PR are below the freezing level (however, it is possible that the real cloud top and small precipitation particles may still be above the freezing level); and 3) minimum TMI 85-GHz PCT > 250 K, where the PFs satisfying this criterion are not expected to have enough precipitation-sized ice particles to depress the microwave radiance at 85 GHz significantly (Spencer et al. 1989; Nesbitt et al. 2000). Note that the rainfall used in this study is derived from the PR with the lowest detectable reflectivity at around 18 dBZ, corresponding to a rainfall rate of about 0.5 mm h^{-1}. Thus, drizzle and light rain from stratocumulus are not detectable by the PR and are not included in the statistics shown here.

The fractions of raining area and rainfall from these warm PFs are calculated and listed in Table 1. Nearly half of the PFs have minimum $T_{B11} > 273$ K and contribute only 13.3% of the raining area and 8% of the

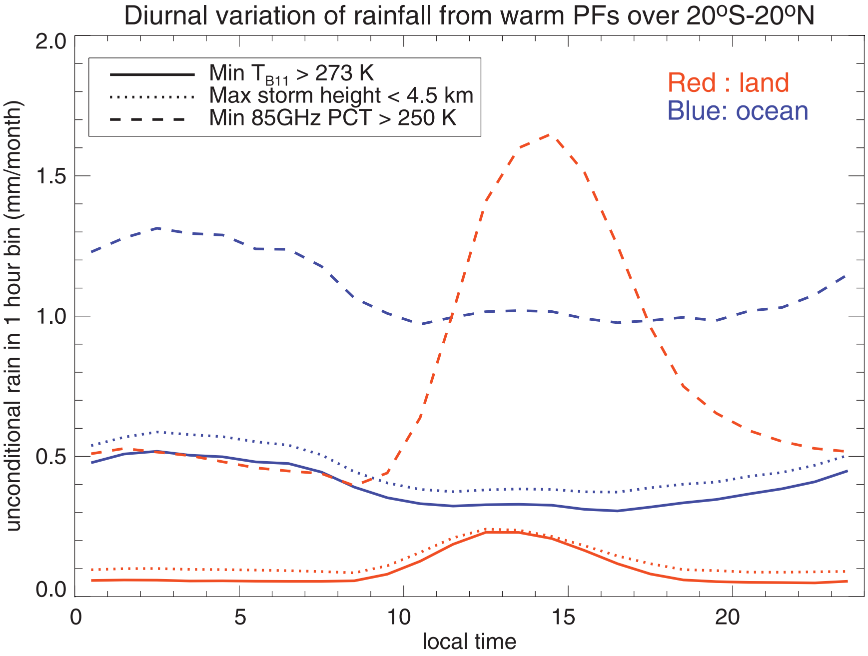

FIG. 6. Diurnal variation of the unconditional rainfall over 20°S–20°N land and ocean from PFs shown in Fig. 1. Units are mm month^{-1} in each local 1-h bin.

total rainfall over the tropics. Sixty-three percent of the PFs with echo top below 4.5 km contribute 16.6% of the raining area and 9.5% of the total rainfall. Most of the PFs (96%) do not have strong microwave ice scattering signatures and contribute 25% of the total rainfall. Note that due to the different scanning geometries of the PR and TMI, there are great difficulties in collocating PR and TMI pixels accurately, which leads to unrealistic minimum 85-GHz PCTs for small and shallow PFs (Liu et al., 2008). Thus, the results from PFs

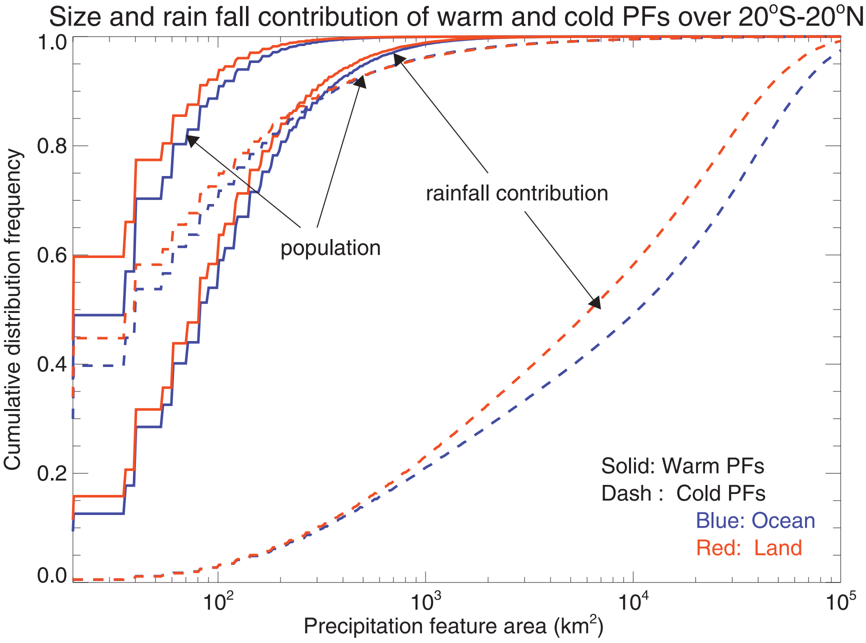

FIG. 7. Cumulative frequency distribution of the population and rainfall contributions of warm PFs with a minimum $T_{B11} > 273$ K and cold PFs with a minimum $T_{B11} < 273$ K.

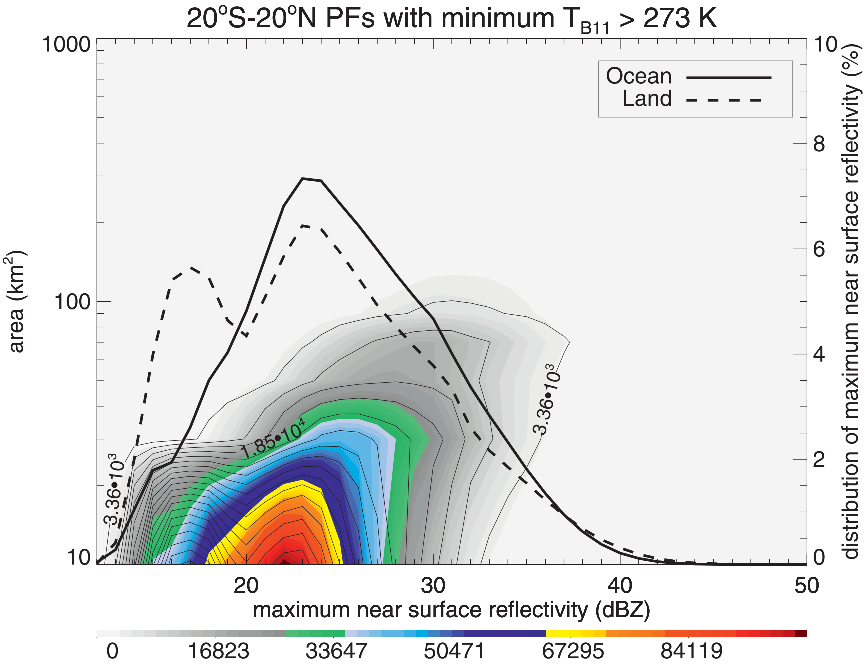

FIG. 8. A 2D histogram of the areas and the maximum near-surface reflectivities of PFs with a minimum VIRS $T_{B11} > 273$ K over 20°S–20°N ocean (color fill) and land (contours). Bin size of the maximum reflectivity is 1 dBZ. Bin size of the PF area is 20 km^2. The histograms of the maximum near-surface reflectivities of PFs over land and ocean are shown with the dashed and thick solid curves.

without microwave ice signatures here need to be interpreted with due caution.

3. Results

First, the geographical distributions of rainfall from these warm PFs are estimated and compared to the amounts of rainfall accumulated from the raining pixels with warm cloud tops. Then, the seasonal and diurnal variations and characteristics of the warm PFs over different regions are discussed. Finally, the seasonal and diurnal variations of the locations of warm PFs with extreme rain volumes are shown.

a. Geographical distribution

Geographical distributions of the unconditional monthly rainfall (total rainfall averaged over all times whether raining or not, as opposed to conditional rain rate by averaging only at times when it is raining) from warm PFs are shown in Fig. 3. The geographical distribution patterns of unconditional rainfall from PFs with minimum $T_{B11} > 273$ K (Fig. 3a) are close to those for PFs with echo tops below 4.5 km (Fig. 3b). Over tropical land, the total amount of rainfall from warm PFs is small. Most warm rainfall occurs over tropical oceans, including the east Pacific ITCZ, the eastern part of the South Pacific convergence zone (SPCZ), the central North Pacific, the South Indian Ocean, and several coastal regions, such as the east coasts of Madagascar, Brazil, Costa Rica, the Philippines, and the Caribbean Islands (Figs. 3a and 3b). For comparison, unconditional rainfall from warm PFs is showed against the total unconditional rainfall from the PR (TRMM 3A25 product) in Figs. 4a and 4b. Regions with large amounts of rainfall from warm PFs have relatively small amounts of total rainfall, except for the Pacific ITCZ (Figs. 4a and 4b). This leads to large proportional contributions of warm PFs in these regions except in the Pacific ITCZ (Figs. 4c and 4d). The contribution of rainfall from warm PFs dominates with more than 50% over the central North Pacific, the central North Atlantic, the central South Indian Ocean, and especially with close to 100% over the region east of the SPCZ. These findings are consistent with earlier studies (Short and Nakamura 2000; Nesbitt et al. 2006).

The amount of unconditional rainfall from PFs with minimum 85-GHz PCT > 250 K is almost twice as much as that from the other two groups of warm PFs (Figs. 3a and 3b). There are at least two reasons for this. First, this group includes some PFs reaching above the 0°C level, but with a low ice water path and without a significant ice-scattering signature. Second, there may be a significant number of small but deep PFs with minimum

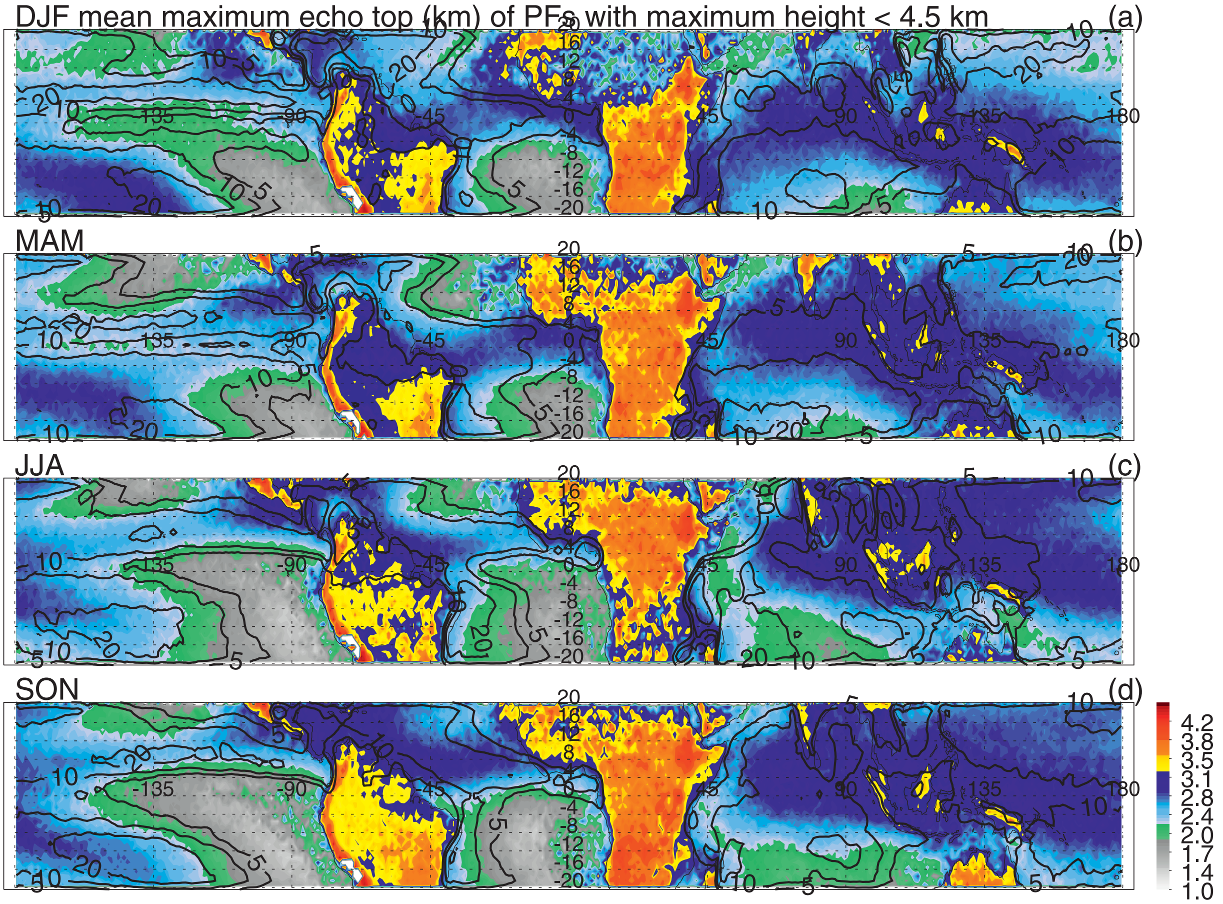

FIG. 9. Seasonal variations of mean maximum 2A23 storm heights (color fill) of PFs with the storm height below 4.5 km. The total unconditional rainfall in Fig. 5 is shown with contours.

85-GHz PCT < 250 K but which are not accurately collocated with the RPF. Over tropical land, some regions have large amounts of rainfall from PFs without an ice-scattering signature, such as the east slope of the Andes and over the Amazon basin. This might lead to an underestimation of the rainfall over these regions by land microwave rainfall retrieval techniques, which mainly depend on the brightness temperature depression at microwave channels caused by ice scattering (Kummerow et al. 2001). Figure 3d shows the differences in the unconditional rainfall resultts from PFs in Figs. 3c and 3a. The rainfall in Fig. 3d is contributed by the PFs with cloud top < 273 K, with small amounts of ice that do not lead to a significant scattering of microwave radiance. These PFs dominate the difference in rainfall over the Amazon, and on the east slope of the Andes.

The mean monthly unconditional rainfall, fractions of raining area, and rainfall from warm PFs are listed for tropical land and ocean separately in Table 2. For comparison, the unconditional rainfall, fractions of raining area and rainfall from all PR pixels with $T_{B11} >$ 273 K, and all PR pixels with collocated TMI 85-GHz PCT > 250 K are listed in Table 2 as well. Over tropical land, on average, only 3 mm month^{-1} and 3% of rainfall are from PFs with warm rain as defined by the IR and radar echo-top criteria. But more than 18 mm month^{-1} and 18% of rainfall are from PFs without a significant ice-scattering signal. About 4% of the raining area is from PFs with minimum $T_{B11} >$ 273 K, but 12.2% of the raining area is from pixels with $T_{B11} >$ 273 K over land. This implies that more than two-thirds of the pixels with cloud tops above the 0°C level are attached to a cold PF over land. Over tropical oceans, only 11.6% of the rainfall is from PFs with their maximum PR echo tops below the 0°C level. This is lower than the 20% of rainfall from pixels with 2A23 storm heights below 4.5 km reported by Short and Nakamura (2000). We suggest that the 8% difference can be interpreted by assuming that nearly half of these low

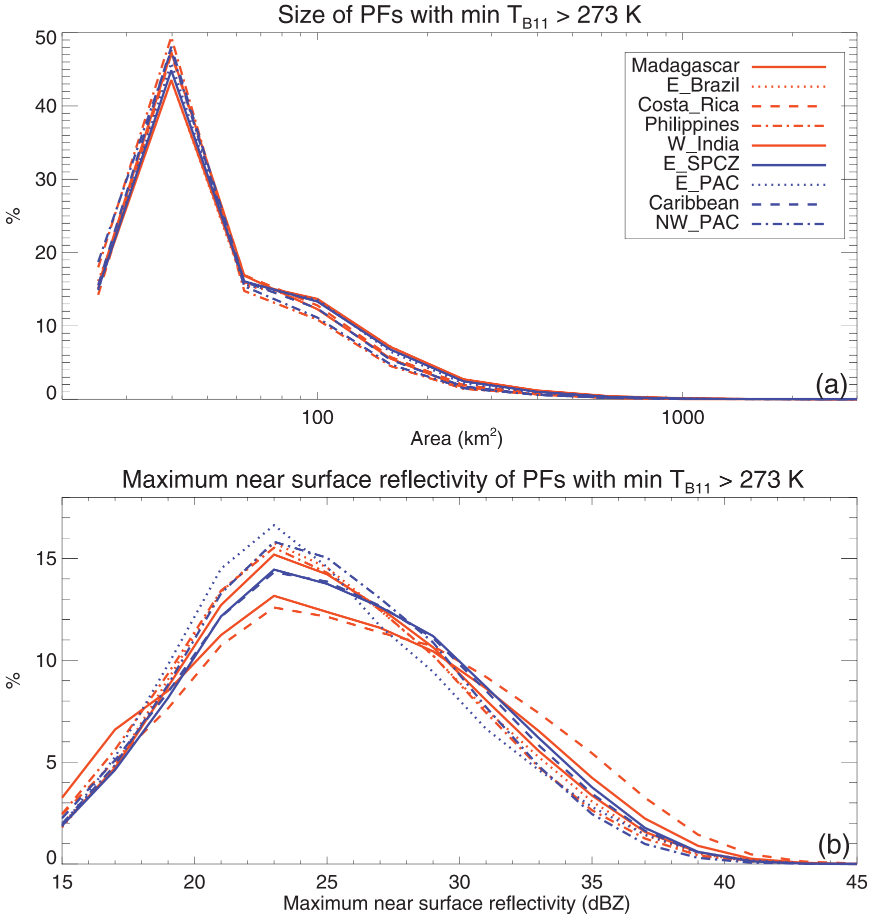

FIG. 10. Histogram of (a) sizes and (b) maximum near-surface reflectivities of PFs with a minimum VIRS $T_{B11} > 273$ K over the selected regions (shown in Fig. 3a).

echo-top pixels are attached to a PF over ocean with adjacent or embedded pixels with echo tops in the ice region. Note that there are large proportions of the raining area and rainfall from pixels without a significant ice-scattering signature, with more over tropical oceans than tropical land.

b. *Seasonal and diurnal variation*

Seasonal variations of unconditional rainfall from PFs with maximum storm heights below 4.5 km are shown in Fig. 5. In general, we may divide warm rain into three groups of regions at different seasons. The first group occurs over the ocean near the coasts. These regions include the east coast of Costa Rica, the Caribbean Islands, the Philippines, and Vietnam in December–February (DJF), as well as the east coast of Brazil, Madagascar, and the west coast of India in June–August (JJA). The shallow PFs contributing to this group of warm rain are likely associated with the inversion caused by the advection of stable conditions by the trade winds (Schubert et al. 1995) and the forcing by topography similar to the line convection near the windward coast of Hawaii (Austin et al. 1996; Carbone et al. 1998). The amounts of warm rainfall over these regions are larger in winter than in summer, with the exception of heavy warm rainfall over the west coast of India during the summer monsoon. The second group occurs all year long over deep oceans including the eastern SPCZ, the central South Indian Ocean, and the central North Pacific. There is a large-scale subsidence over these basically trade wind regions. The seasonal migration of the warm rainfall from this group is associated with the sea surface temperature and the strength of the subsidence. The PFs associated with this scenario are more likely to be the buoyant plumes balancing the latent and sensible heat fluxes rising from the sea surface (Houze 1993). The third group occurs all year long over very rainy regions including the central Pacific and the Atlantic ITCZ. Note that there is a large amount of warm rainfall over the secondary southern ITCZ during March–May

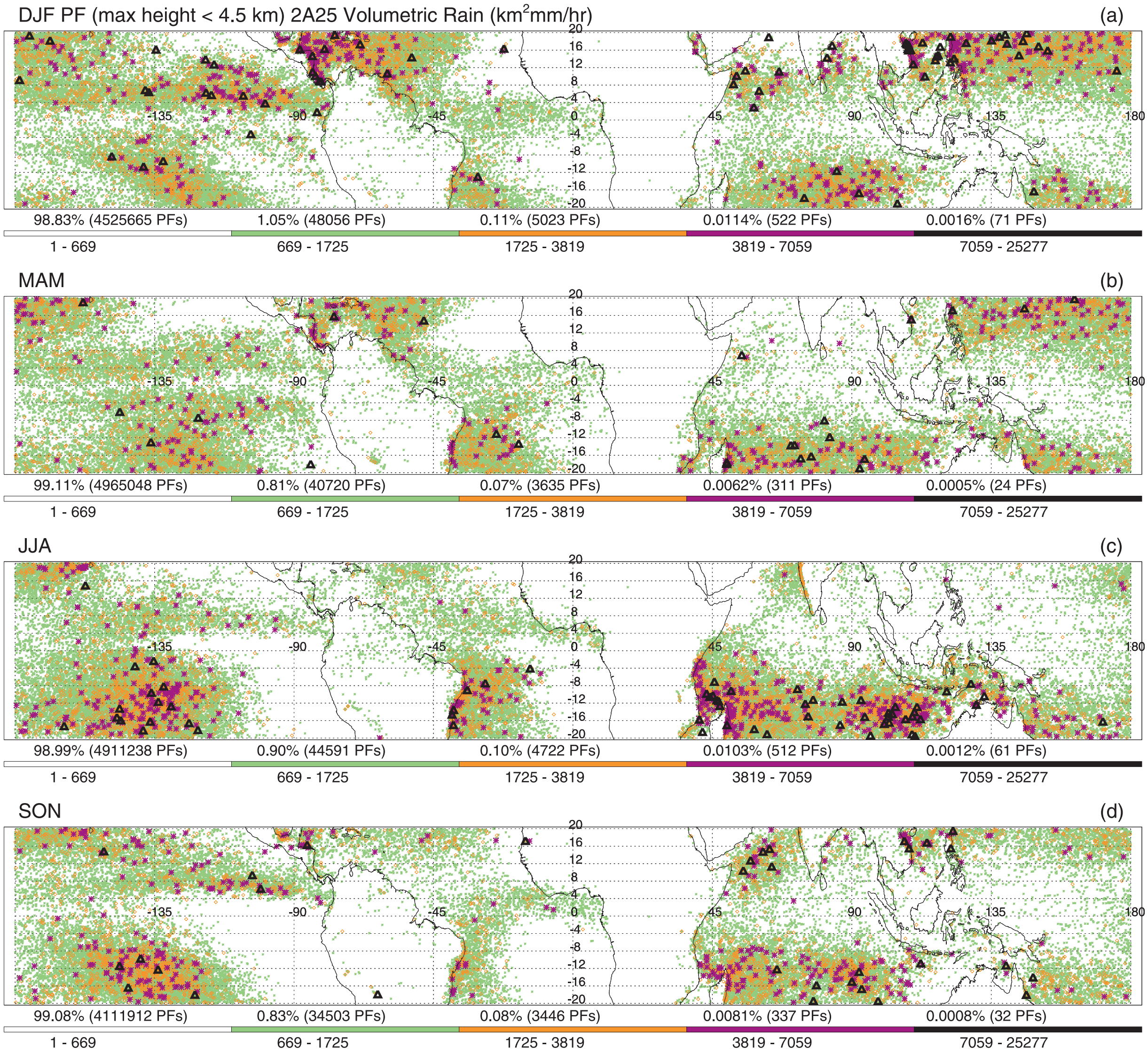

FIG. 11. Seasonal variations of the locations of PFs with a maximum storm height < 4.5 km categorized by their volumetric rainfall. Rarity of the events is represented by colored symbols: green, ~ top 1%; orange, ~ top 0.1%; purple, ~ top 0.01%; and black, ~ top 0.001%. The same value ranges are used for different seasons.

(MAM) (Zhang 2001). The mechanism for the shallow PFs associated with this group is uncertain.

The diurnal variations of the unconditional rainfall from the PFs listed in Table 1 are shown in Fig. 6. Over land, the amount of warm rainfall reaches its maximum in the early afternoon. Some of these warm PFs are small cumuli at very early stages of deep convection. There is about a 1-h time lag between the rainfall from PFs with minimum 85-GHz PCT $>$ 250 K and other warm PFs. This may be explained as a result of PFs with some ice that nonetheless satisfy the criterion that the minimum 85-GHz PCT $>$ 250 K, but are missed by the IR or PR criteria due to the collocation problem. Over oceans, the diurnal cycle of warm rainfall is weak, and more warm rainfall happens during the nighttime than the daytime. These results are consistent with the diurnal cycles of population and conditional rainfall from PFs without an ice-scattering signature, as shown by Nesbitt and Zipser (2003). The total rainfall from PFs with warm cloud tops and with radar echo tops below freezing over tropical oceans is greater than that over tropical land at any and all times.

c. *Characteristics of warm rain systems*

The cumulative distribution frequencies (CDFs) of the population and rainfall contributions of warm PFs

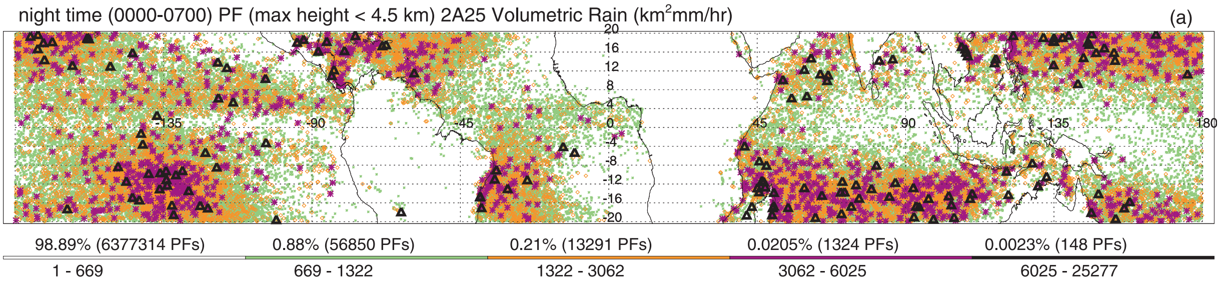
night time (0000-0700) PF (max height < 4.5 km) 2A25 Volumetric Rain (km^{2}mm/hr)

day time (1000-1700)

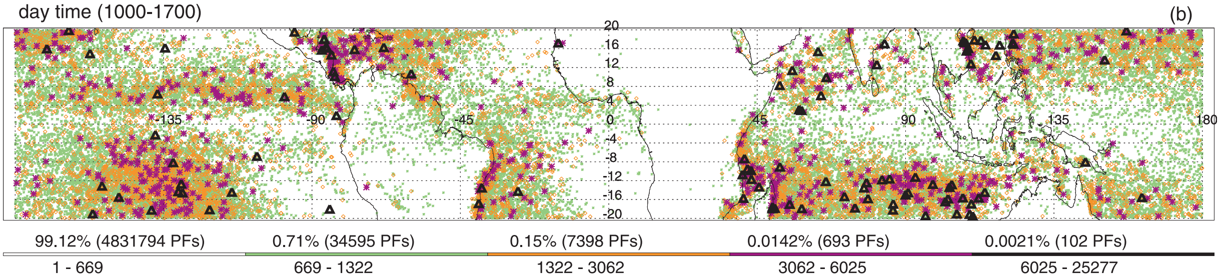

FIG. 12. Day vs night variations of the locations of PFs with a maximum storm height < 4.5 km categorized by their volumetric rainfall. Rarity of the events is represented with green, orange, purple, and black symbols using the same value ranges as in Fig. 11.

with minimum $T_{B11} > 273$ K and cold PFs with minimum $T_{B11} < 273$ K with different sizes are shown in Fig. 7. About 90% of the warm PFs have sizes smaller than 100 km^2 and they contribute about 50% of the warm rainfall over both tropical land and ocean. Warm PFs over ocean are only slightly larger than over land. There is no significant difference between the rainfall contribution or size dependence from PFs over ocean and those from PFs over land. In general, warm PFs with larger size have higher maximum near-surface reflectivities (Fig. 8). Warm PFs have their modal maximum near-surface reflectivities around 23 dBZ over both land and ocean, corresponding to a 0.08 g m^{-3} rainwater content and a 1.3 mm h^{-1} rain rate if using the radar reflectivity and water mass relation of Tokay and Short (1996). However, there are some PFs with maximum near-surface reflectivities of up to 45 dBZ, corresponding to ~2.0 g m^{-3} and 44 mm h^{-1} (Figs. 2 and 8). There is a second peak of maximum reflectivity at 17 dBZ from warm PFs over land in Fig. 8. Since most of these PFs have sizes of about 20 km^2 (only one PR pixel), and 17 dBZ is near the margin of PR sensitivity, this peak might be caused by the noisy signal over land. Though there are about 3% of warm PFs with maximum near-surface reflectivities of less than 17 dBZ, they only contribute 0.3% of the total warm rainfall.

The mean maximum storm heights of warm PFs with echo tops below 4.5 km are shown for different seasons in Fig. 9. Over most tropical land areas, the mean storm heights of warm PFs are about 4 km. Some of these PFs are likely to develop into deeper convection later. One exception is that the mean storm heights of warm PFs over the Amazon are about 1 km lower. This implies that there are large numbers of PFs with relatively low echo tops over the region. This is consistent with the "green ocean" concept of the Amazon (Silva Dias et al. 2002) that the convection in the region exhibits some of the properties of oceanic convection. Over tropical oceans with large amounts of warm rainfall, including the regions near the coasts, the mean storm heights of warm PFs are lower than 3 km. The pattern of a gradual increase of height of warm PFs is consistent with the deepening of the base of the inversion layer toward the ITCZ and SPCZ over increasing sea surface temperature and decreasing large-scale subsidence.

The size and intensity of warm PFs over different regions (Fig. 3a) are shown in Fig. 10. There are no significant differences among the sizes and the maximum near-surface reflectivities of the PFs over the selected regions. There is almost no difference among the diurnal cycles of the warm rainfall over different ocean regions. Land regions have a similar diurnal cycle pattern as shown in Fig. 6. The only exception is that warm rain over the land area of Madagascar maximizes about 1 h later than in other regions (figure not shown).

d. *Extreme warm rain events*

The locations of warm PFs categorized by their rarity of large volumetric rain are shown seasonally in Fig. 11. Many heavily raining warm PFs are located near the windward coasts, with more in winter than in summer. Many of these PFs have a quasi-linear shape along the coast, like the example shown in Figs. 2a–c. Similar to the trade wind clouds east of Hawaii (Carbone et al. 1998), these PFs bring heavy rainfall to windward coasts, especially those with significant topography. Some other heavily raining warm PFs are located in the eastern SPCZ, and the South Indian Ocean and eastern Pacific ITCZ. These PFs are mostly mesoscale cellular convection, as is the example shown in Figs. 2d–f. It is interesting to notice that there are a few warm PFs with heavy rainfall over the Arabian Sea in September–November (SON) and DJF. Heavy rainfall from warm PFs occurs more often during nighttime than daytime. There are about twice as many warm PFs with volumetric rain greater than 1322 $\mathrm{km}^2\ \mathrm{mm}\ \mathrm{h}^{-1}$ during the nighttime than during the daytime (Fig. 12).

4. Summary

- Raining pixels with cloud-top temperatures $> 0°\mathrm{C}$ contribute 20% of total rainfall over tropical oceans and 7.5% over tropical land. However, about half of these pixels over ocean and two-thirds of those over land are attached to cold precipitation systems.
- Large amounts of warm rainfall occur over oceans near windward coasts during winter.
- Most of the warm rain systems are of small size, $< 100\ \mathrm{km}^2$, and weak radar echoes with modal maximum values of about 23 dBZ. However, mesoscale warm rain systems with strong radar echoes are distributed around the tropical oceans, with more during nighttime than during daytime.
- The mean heights of warm PFs over ocean are lower than for warm PFs over land.
- There is no significant regional difference in the sizes and intensities of warm PFs in the tropics.

There are two ambiguities in interpreting warm rain by using TRMM PFs. First, TRMM does not observe the raining systems continuously; it only provides snapshots and there is no historical information about PFs. It is possible that some warm dissipating PFs originating from cold systems are included as warm PFs. Second, the drizzle and light rain in stratocumulus are not detectable by the PR and are not included in the statistics shown here. CloudSat can detect very light rainfall (e.g., Stephens and Haynes 2007) and will be able to provide a better assessment of the distribution and properties of light rainfall. The present results should be useful for evaluating the occurrence and representation of warm rain processes in global climate and numerical weather prediction models.

Acknowledgments. This research was supported by NASA Precipitation Measurement Mission Grant NAG5-13628 under the direction of Dr. Ramesh Kakar. Thanks to two anonymous reviewers and Dr. Steven Krueger for valuable suggestions. Special thanks go to Drs. Erich Stocker and John Kwiatkowski and the rest of the TRMM Science Data and Information System (TDSIS) team at NASA Goddard Space Flight Center, Greenbelt, Maryland, for data processing assistance.

REFERENCES

Augstein, E., H. Riehl, F. Ostapoff, and V. Wagner, 1973: Mass and energy transports in an undisturbed Atlantic trade-wind flow. *Mon. Wea. Rev.,* **101,** 101–111.

Austin, G. R., R. M. Rauber, H. T. Ochs III, and L. J. Miller, 1996: Trade-wind clouds and Hawaiian rainbands. *Mon. Wea. Rev.,* **124,** 2126–2151.

Awaka, J., T. Iguchi, and K. Okamoto, 1998: Early results on rain type classification by the Tropical Rainfall Measuring Mission (TRMM) precipitation radar. *Proc. Eighth URSI Commission F Open Symp.,* Aveiro, Portugal, International Union of Radio Science, 143–146.

Baker, M., 1993: Trade cumulus observations. *The Representation of Cumulus Convection in Numerical Models, Meteor. Monogr.,* No. 46, Amer. Meteor. Soc., 29–37.

Bretherton, C. S., and Coauthors, 2004: The Epic 2001 Stratocumulus Study. *Bull. Amer. Meteor. Soc.,* **85,** 967–977.

Carbone, R. E., J. D. Tuttle, W. A. Cooper, V. Grubisic, and W. C. Lee, 1998: Trade wind rainfall near the windward coast of Hawaii. *Mon. Wea. Rev.,* **126,** 2847–2863.

Houze, R. J., 1993: *Cloud Dynamics*. International Geophysics Series, Vol. 53, Academic Press, 572 pp.

Iguchi, T., T. Kozu, R. Meneghini, J. Awaka, and K. Okamoto, 2000: Rain-profiling algorithm for the TRMM Precipitation Radar. *J. Appl. Meteor.,* **39,** 2038–2052.

Kummerow, C., W. Barnes, T. Kozu, J. Shiue, and J. Simpson, 1998: The Tropical Rainfall Measuring Mission (TRMM) sensor package. *J. Atmos. Oceanic Technol.,* **15,** 809–817.

——, and Coauthors, 2001: The Evolution of the Goddard Profiling Algorithm (GPROF) for rainfall estimation from passive microwave sensors. *J. Appl. Meteor.,* **40,** 1801–1820.

Liu, C., E. Zipser, D. Cecil, S. W. Nesbitt, and S. Sherwood, 2008: A cloud and precipitation feature database from nine years of TRMM observations. *J. Appl. Meteor. Climatatol.,* **47,** 2712–2728.

Liu, G., J. A. Curry, and R.-S. Sheu, 1995: Classification of clouds over the western equatorial Pacific Ocean using combined infrared and microwave satellite data. *J. Geophys. Res.,* **100,** 13 811–13 826.

Malkus, J. S., 1954: Some results of a trade cumulus cloud investigation. *J. Atmos. Sci.,* **11,** 220–237.

——, 1955: On the formation and structure of downdrafts in cumulus clouds. *J. Atmos. Sci.,* **12,** 350–354.

Nesbitt, S. W., and E. J. Zipser, 2003: The diurnal cycle of rainfall and convective intensity according to three years of TRMM measurements. *J. Climate,* **16,** 1456–1475.

——, ——, and D. J. Cecil, 2000: A census of precipitation features in the Tropics using TRMM: Radar, ice scattering, and lightning observations. *J. Climate,* **13,** 4087–4106.

——, R. Cifelli, and S. Rutledge, 2006: Storm morphology and rainfall characteristics of TRMM precipitation features. *Mon. Wea. Rev.,* **134,** 2702–2721.

Nitta, T., and S. Esbensen, 1974: Heat and moisture budget analyses using BOMEX data. *Mon. Wea. Rev.,* **102,** 17–28.

Petty, G. W., 1999: Prevalence of precipitation from warm-topped clouds over eastern Asia and western Pacific. *J. Climate,* **12,** 220–229.

Rauber, R. M., and Coauthors, 2007: Rain in shallow cumulus over the ocean: The RICO campaign. *Bull. Amer. Meteor. Soc.,* **88,** 1912–1928.

Schubert, W. H., P. E. Ciesielski, C. Lu, and R. H. Johnson, 1995: Dynamical adjustment of the trade wind inversion layer. *J. Atmos. Sci.,* **52,** 2941–2952.

Schumacher, C., and R. A. Houze Jr, 2003: The TRMM Precipitation Radar's view of shallow, isolated rain. *J. Appl. Meteor.,* **42,** 1519–1524.

Short, D. A., and K. Nakamura, 2000: TRMM radar observations of shallow precipitation over the tropical oceans. *J. Climate,* **13,** 4107–4124.

Silva Dias, M. A. F., and Coauthors, 2002: Cloud and rain processes in a biosphere–atmosphere interaction context in the Amazon region. *J. Geophys. Res.,* **107,** 8072, doi:10.1029/2001JD000335.

Simpson, J., M. Garstang, E. J. Zipser, and G. A. Dean, 1967: A study of a non-deepening tropical disturbance. *J. Appl. Meteor.,* **6,** 237–254.

Spencer, R. W., H. G. Goodman, and R. E. Hood, 1989: Precipitation retrieval over land and ocean with the SSM/I: Identification and characteristics of the scattering signal. *J. Atmos. Oceanic Technol.,* **6,** 254–273.

Stephens, G. L., and J. M. Haynes, 2007: Near global observations of the warm rain coalescence process. *Geophys. Res. Lett.,* **34,** L20805, doi:10.1029/2007GL030259.

Tokay, A., and D. A. Short, 1996: Evidence from tropical raindrop spectra of the origin of rain from stratiform versus convective clouds. *J. Appl. Meteor.,* **35,** 355–371.

Zhang, C., 2001: Double ITCZs. *J. Geophys. Res.,* **106,** 11 785–11 792.